Rotating electroosmotic flow in a non-uniform microchannel

Cheng Qi[a], Chiu-On Ng[b1]

[a]Hubei Key Laboratory of Theory and Application of Advanced Materials Mechanics, Wuhan University of Technology, Wuhan 430070, China

[b]Department of Mechanical Engineering, The University of Hong Kong, Pokfulam Road, Hong Kong

July 26, 2018

Abstract

An analytical model based on lubrication approximation is developed for rotating electroosmotic flow in a narrow slit channel, of which the wall shape and surface potential may vary slowly in the direction of applied fields. The primary and secondary flow fields and the induced pressure gradient, which vary periodically with axial position owing to the gradually varied channel height and surface potentials, are deduced as functions of the inverse Ekman number and the Debye parameter. By studying some limiting cases of special interest, the combined effects of system rotation and the interaction between the geometrical and potential variations are investigated. It is shown that non-uniformity in the channel height and wall potential can qualitatively modify the relationship between system rotation and the primary and secondary flow rates.

Keywords: electroosmotic flow; rotating channel; Ekman layer; lubrication approximation.

[1]Corresponding author. Tel: +(852) 3917 2622; Fax: +(852) 2858 5415; E-mail address: cong@hku.hk (C.-O. Ng).

1 Introduction

Fluid pumping is an essential function in microfluidic systems [1]. In recent years, electroosmotic pumps have been increasingly employed to perform this function [2,3]. When an electric potential difference is applied between the ends of a channel, fluid will be driven into motion by electric body force, which arises because of free charges in the near-wall electric double layer (EDL). The thickness of the EDL depends on the bulk ionic concentration and electrical properties of the electrolyte [4]. Outside the EDL where the electric body force is absent due to charge neutrality, bulk flow is induced by viscous action. Pure electroosmotic (EO) flow in uniform channels has the feature that its velocity profile is plug-like (a constant velocity over the cross-section except within the EDL close to the channel wall). As a result, Taylor dispersion of solutes is negligible in pure EO flow [5], which is desirable for electrophoretic separation of chemical species but undesirable for mixing. Electroosmosis counts on the existence of interfacial charges at solid/liquid interface, which can be affected by a variety of mechanisms such as ionization of solid surface groups and isomorphic substitution [6, 7].

Another technique for moving small quantity of fluids in narrow confinements is by means of centrifugal force in a rotating system, which is frequently utilized in the so-called compact disc (CD)-based microfluidics. As centrifugal pumping is relatively insensitive to physicochemical properties such as pH, ionic strength, or chemical composition of solutions (in contrast to EO-based pumps), a CD-based system may manipulate broader types of liquids. Aqueous solutions, solvents, surfactants, and biological fluids (blood, milk, and urine) have all been pumped successfully [8]. Due to significant hydrodynamic dispersion produced by system rotation, mixing in CD-based microfluidic devices can be easily achieved. Unlike EO flow, which is determined by many parameters, the control of flow in CD-based microfluidics lacks flexibility, however. Its only control is the spinning speed, and the rest is left to a complicated circuitry involving hydrophobic burst valves to be hardwired on a CD [9]. To make full use of advantages offered by both EO and centrifugal pumping, a dual-pumping system can be developed. Wang et al. [10] designed a dual-pumping CD-like microfluidic system aiming at improving biomedical separation efficiency. The fundamental principle of their design was to make electric body force acting in a direction opposite to the centrifugal force. Their system was found to have other advantages like low joule-heat generation, low

chemistry reaction and steady ion concentration [10]. Chakraborty [11] can be consulted for details about the centrifugal microfluidics.

Chang and Wang [12] were among the first to present a theoretical study on rotating EO flow. They derived analytical solutions in terms of the rotation speed and the Debye parameter for two configurations, namely, flow over a single plate and flow between two parallel flat plates. More recently, Ng and Qi [9] considered EO flow in a rotating rectangular channel. They developed semi-analytical solutions in terms of eigenfunction expansions for the primary and secondary EO flow velocities as functions of the the inverse Ekman number and the Debye parameter. It was shown that system rotation can have qualitatively different effects on the flow rate, depending on the channel width and wall potential distributions. Ng and Qi [9] also examined in detail the Ekman–EDL layer, which is a boundary layer incorporating the Coriolis, electrical and viscous forces, and develops under the conditions of fast rotation and a thin EDL. Other studies concerning rotating EO flow of non-Newtonian fluids, such as power-law, third grade, Eyring, viscoplastic and viscoelastic materials, have also been conducted [13–20].

In the above-mentioned studies, only uniform channels (i.e., conditions do not vary with axial position) are considered. Arising either by construction or naturally, non-uniformity in the channel height and wall potential distribution is often a key consideration in the study of EO flows. For example, the surface charge may be non-uniformly distributed owing to the absorption of organic molecules onto the channel wall during analysis [21, 22]. To enhance chemical/biochemical reactions on sensing surfaces [23] or the efficiency of species mixing [24] in lab-on-a-chip applications, the channel walls can be artificially patterned with rough elements in order to achieve a stronger mixing effect. In a rotating environment, EO flow will be determined by a balance between the viscous, Lorentz and Coriolis forces. Any non-uniformity in the channel height and wall potential will give rise to an induced pressure gradient, which will then add to the other forces to affect the flow.

In the literature, there exist many studies on EO flow under the effect of surface patterning. Stroock et al. [25] found in their experiments the formation of recirculating cellular flow over a surface which was periodically patterned with equal positive–negative potentials. The induced pressure gradient arising from the non-uniform surface charge distribution can only

produce convective cells without a net flow. To generate a net flow, one can introduce wall undulation. Ajdari [26, 27] has theoretically shown that, with the combined effect of wall undulation and charge modulation, the symmetry of forward–backward flow can be broken and a net flow is produced. Yang and Liu [28] performed a numerical study on EO flow in a parallel-plate microchannel with sinusoidal roughness, and looked into the effect of roughness height and frequency on the bulk flow rate.

To this date, rotating EO flow subject to non-uniformity in both channel height and surface potential has not been studied. Shit et al. [29] have investigated the effects of slip velocity on rotating EO flow in a non-uniform channel with wavy walls. They have, however, ignored in their analysis the internally induced pressure gradient arising from the varying channel height. In this paper, our aim is to develop an analytical model to describe EO flow in a narrow slit channel under the combined effect of system rotation and non-uniformity in both the channel height and wall potentials. It is assumed that the wall shape and potential may vary slowly in the axial direction and the inertia is negligible. Under these conditions, the lubrication theory can be applied to the problem, which is then solved in a quasi-one-dimensional manner. Many previous studies have applied the lubrication theory to EO flow in thin channels, including Long et al. [30], Ajdari [31], Ghosal [32], Ng and Zhou [33], Ng and Qi [34], Qi and Ng [35, 36], and so on.

Our problem and method of solution are described in further detail in Section 2, where the primary and secondary flow velocities, as well as the induced pressure gradient, are derived as functions of the dimensionless rotation and Debye parameters. Further assuming sinusoidal functions for the wall shape and potential distribution, we consider some cases of particular interest in Section 3. These cases include: non-rotating channel, channel with constant sectional area, very thin Ekman and EDL layers, uncharged flat lower wall, and symmetric wall patterns. Through these cases, we shall look into how the interaction between the variations in the wall shape and potential on the walls may give rise to certain interesting phenomena, and how the system rotation may modify these phenomena. Results of particular cases are compared with those available in the literature. We shall place emphasis on results that distinguish rotating EO flow in a non-uniform channel from that in a uniform channel. Most findings of the present study are reported for the first time.

2 Problem formulation and solution

Our problem is to consider steady pressure-driven and electroosmotic flow in a rotating slit microchannel, where the wall shape and the surface potential may vary slowly and periodically as functions of axial position. As is shown in Fig. 1, flow is primarily driven under the combined action of a pressure gradient and an electric field applied along the x-direction, and because of system rotation about the z-axis, secondary flow arises in the transverse y-direction. Here, the coordinates (x, y, z) follow the right-hand rule, and hence rotation is positive anti-clockwise when viewed from above. The channel, which rotates at a constant speed Ω, is assumed to be wide and open-ended in the y-direction so that the flow can be assumed to be invariant in this direction. Hence, the flow is a function of the x- and z-coordinates only.

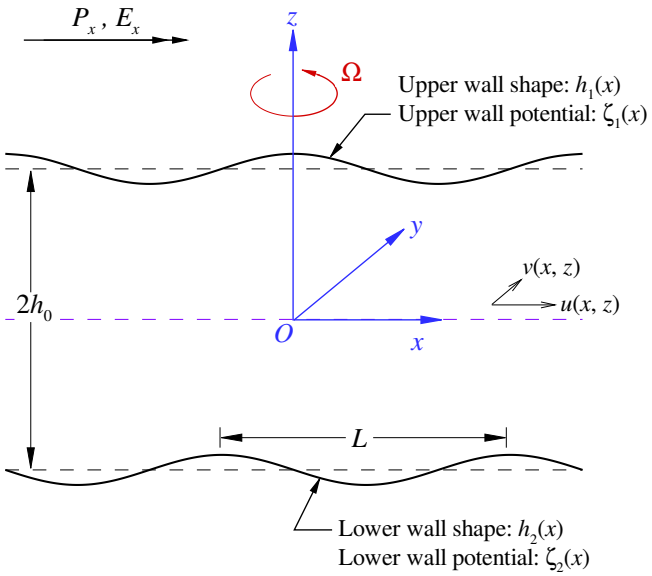

Figure 1: Electroosmotic flow through a rotating slit channel with gradually varying wall shape and wall potential.

The upper and lower walls are placed at $z = h_1(x)$ and $z = -h_2(x)$, respectively, where $h_1(x)$ and $h_2(x)$ have the same mean: $\langle h_1 \rangle = \langle h_2 \rangle = h_0$, in which the angle brackets denote averaging over one wavelength in the x-direction. In other words, each wall is at a mean

distance of h_0 from the centerline of the channel, and therefore the channel has an average height of $2h_0$. On the upper and lower walls, the surface potentials are given by $\zeta_1(x)$ and $\zeta_2(x)$, respectively. The wall positions $h_{1,2}(x)$ and the surface potentials $\zeta_{1,2}(x)$ are all periodic functions of x with the same wavelength L, which is assumed to be much longer than the channel height h_0, or $\varepsilon \equiv h_0/L \ll 1$. Such a small length ratio means a much longer length scale for velocity variations in the x-direction than that in the z-direction, and hence velocity gradients with respect to x will be much smaller than those with respect to z. In addition to the sharp contrast in the length scales, we also assume that the Reynolds number Re of the flow is so small that $\varepsilon Re \ll 1$ for negligible inertia terms. These two conditions, one geometric and one dynamic, will form the basis for the so-called lubrication approximation; see, e.g., Deen [37].

On ignoring gravity, and applying the lubrication approximation, the momentum equations for the rotating flow can be written as follows:

$$-2\rho\Omega v = \mu\frac{\partial^2 u}{\partial z^2} + \rho_e E_x + P_x, \tag{1}$$

$$2\rho\Omega u = \mu\frac{\partial^2 v}{\partial z^2}, \tag{2}$$

where ρ is the fluid density, μ is the dynamic viscosity of the fluid, $u = u(x, z)$ and $v = v(x, z)$ are the velocity components in x- and y-directions, ρ_e is the free charge density in the fluid, E_x is the electric field applied purely along the x-direction, and $P_x = P_x(x) = -\mathrm{d}p/\mathrm{d}x$ is the reduced pressure gradient consisting of the externally applied and internally induced components. The condition $\varepsilon \ll 1$ implies that the flow is nearly parallel to the axis of the channel, or the velocity component in the z-direction is much smaller in magnitude than the other velocity components.

The electric potential ψ is related to the free charge density ρ_e through the following Poisson equation:

$$\rho_e = -\epsilon\frac{\mathrm{d}^2\psi}{\mathrm{d}z^2}, \tag{3}$$

where ϵ is the dielectric permittivity of the fluid. It is assumed that the valence Z of the charges is $1:1$ symmetric, and ions in the EDL follow a Boltzmann distribution. As a result, the free charge density can be written as

$$\rho_e = -2Zen_\infty \sinh\left(\frac{Ze\psi}{k_B T}\right), \tag{4}$$

where e is the fundamental charge, n_∞ is the bulk electric concentration, k_B is the Boltzmann constant, and T is the absolute temperature. By invoking the Debye–Hückel approximation on assuming that the potential is so small that $\sinh(Ze\psi/k_BT) \approx Ze\psi/k_BT$, Eqs. (3) and (4) together give the well-known linearized Poisson–Boltzmann equation:

$$\frac{\mathrm{d}^2\psi}{\mathrm{d}z^2} = \kappa^2\psi, \tag{5}$$

where $\kappa = (2Z^2e^2n_\infty/\epsilon k_BT)^{1/2}$ is the Debye parameter, the inverse of which is the Debye shielding length of the EDL. The electric potential is subject to the following boundary conditions:

$$\psi = \zeta_1, \text{ at } z = h_1, \tag{6}$$

$$\psi = \zeta_2, \text{ at } z = -h_2, \tag{7}$$

where $\zeta_1 = \zeta_1(x)$ and $\zeta_2 = \zeta_2(x)$ are the surface potentials on the upper and lower walls. Equation (5) with these boundary conditions can be readily solved to give

$$\psi = \frac{\zeta_1 \sinh\left[\kappa\left(z + h_2\right)\right]}{\sinh\left[\kappa\left(h_1 + h_2\right)\right]} + \frac{\zeta_2 \sinh\left[\kappa\left(h_1 - z\right)\right]}{\sinh\left[\kappa\left(h_1 + h_2\right)\right]}, \tag{8}$$

or in dimensionless form

$$\hat{\psi} = \frac{\hat{\zeta}_1 \sinh\left[\hat{\kappa}\left(\hat{z} + \hat{h}_2\right)\right]}{\sinh\left[\hat{\kappa}\left(\hat{h}_1 + \hat{h}_2\right)\right]} + \frac{\hat{\zeta}_2 \sinh\left[\hat{\kappa}\left(\hat{h}_1 - \hat{z}\right)\right]}{\sinh\left[\hat{\kappa}\left(\hat{h}_1 + \hat{h}_2\right)\right]}, \tag{9}$$

where the dimensionless variables and parameters are defined as follows:

$$(\hat{\psi}, \hat{\zeta}_1, \hat{\zeta}_2) = (\psi, \zeta_1, \zeta_2)/\zeta_0, \quad (\hat{z}, \hat{h}_1, \hat{h}_2) = (z, h_1, h_2)/h_0, \quad \hat{\kappa} = \kappa h_0, \tag{10}$$

in which ζ_0 and h_0 are the normalization scales for the potentials and lengths, respectively. As noted above, $h_0 = \langle h_1 \rangle = \langle h_2 \rangle$ is half the mean channel height. Likewise, we may choose either $\langle \zeta_1 \rangle$ or $\langle \zeta_2 \rangle$ (if they are not both zero) to be the scale ζ_0.

It follows from Eqs. (3) and (5) that $\rho_e = -\epsilon\kappa^2\psi$. The electric body force $\rho_e E_x$ in the momentum equation (1) can then be expressed as $\rho_e E_x = -\epsilon\kappa^2 E_x\psi$. To facilitate our analysis, we further introduce the following dimensionless variables:

$$(\hat{u}, \hat{v}) = (u, v)/U_{\text{HS}}, \quad \hat{P}_x = P_x h_0^2/(\mu U_{\text{HS}}), \quad \hat{x} = x/L, \tag{11}$$

where the velocity scale

$$U_{\rm HS} = -\epsilon\zeta_0 E_x/\mu \tag{12}$$

has the same form as the Helmholtz–Smoluchowski velocity. In terms of the dimensionless variables, the momentum equations (1) and (2) become

$$-2\eta^2\hat{v} = \frac{\partial^2\hat{u}}{\partial\hat{z}^2} + \hat{P}_x + \hat{\kappa}^2\hat{\psi}, \tag{13}$$

$$2\eta^2\hat{u} = \frac{\partial^2\hat{v}}{\partial\hat{z}^2}, \tag{14}$$

where

$$\eta = \left(\frac{\rho h_0^2\Omega}{\mu}\right)^{1/2} \tag{15}$$

is a dimensionless rotation parameter, or the square root of the inverse Ekman number [38].

With the no-slip condition at the walls: $\hat{u} = \hat{v} = 0$ at $\hat{z} = \hat{h}_1$ and $\hat{z} = -\hat{h}_2$, the momentum equations can be solved to yield

$$\begin{aligned}\hat{u}(\hat{x},\hat{z}) &= -\left(\frac{\hat{\kappa}^4}{\hat{\kappa}^4+4\eta^4}\right)\hat{\psi} - W_1\left(\frac{\hat{P}_x}{2\eta^2}\right) + \left(\frac{\hat{\kappa}^4}{\hat{\kappa}^4+4\eta^4}\right)\left(W_3\hat{\zeta}_1 + W_4\hat{\zeta}_2\right) \\ &\quad - \left(\frac{2\eta^2\hat{\kappa}^2}{\hat{\kappa}^4+4\eta^4}\right)\left(W_5\hat{\zeta}_1 + W_6\hat{\zeta}_2\right),\end{aligned} \tag{16}$$

$$\begin{aligned}\hat{v}(\hat{x},\hat{z}) &= -\left(\frac{2\eta^2\hat{\kappa}^2}{\hat{\kappa}^4+4\eta^4}\right)\hat{\psi} + (W_2-1)\left(\frac{\hat{P}_x}{2\eta^2}\right) + \left(\frac{\hat{\kappa}^4}{\hat{\kappa}^4+4\eta^4}\right)\left(W_5\hat{\zeta}_1 + W_6\hat{\zeta}_2\right) \\ &\quad + \left(\frac{2\eta^2\hat{\kappa}^2}{\hat{\kappa}^4+4\eta^4}\right)\left(W_3\hat{\zeta}_1 + W_4\hat{\zeta}_2\right),\end{aligned} \tag{17}$$

where

$$\begin{aligned}W_1 &= 2\left\{\sin\left[\eta\left(\hat{z}-\hat{h}_1\right)\right]\sinh\left[\eta\left(\hat{z}+\hat{h}_2\right)\right] + \sin\left[\eta\left(\hat{z}+\hat{h}_2\right)\right]\sinh\left[\eta\left(\hat{z}-\hat{h}_1\right)\right]\right\} \\ &\quad \times\left\{\frac{\cos\left[\eta\left(\hat{h}_1+\hat{h}_2\right)\right] - \cosh\left[\eta\left(\hat{h}_1+\hat{h}_2\right)\right]}{\cos\left[2\eta\left(\hat{h}_1+\hat{h}_2\right)\right] - \cosh\left[2\eta\left(\hat{h}_1+\hat{h}_2\right)\right]}\right\},\end{aligned} \tag{18}$$

$$\begin{aligned}W_2 &= 2\left\{\cos\left[\eta\left(\hat{z}-\hat{h}_1\right)\right]\cosh\left[\eta\left(\hat{z}+\hat{h}_2\right)\right] + \cos\left[\eta\left(\hat{z}+\hat{h}_2\right)\right]\cosh\left[\eta\left(\hat{z}-\hat{h}_1\right)\right]\right\} \\ &\quad \times\left\{\frac{\cos\left[\eta\left(\hat{h}_1+\hat{h}_2\right)\right] - \cosh\left[\eta\left(\hat{h}_1+\hat{h}_2\right)\right]}{\cos\left[2\eta\left(\hat{h}_1+\hat{h}_2\right)\right] - \cosh\left[2\eta\left(\hat{h}_1+\hat{h}_2\right)\right]}\right\},\end{aligned} \tag{19}$$

$$
\begin{aligned}
W_3 &= \left\{\cos\left[\eta\left(\hat{z}+\hat{h}_1+2\hat{h}_2\right)\right]\cosh\left[\eta\left(\hat{z}-\hat{h}_1\right)\right]\right. \\
&\quad \left.-\cos\left[\eta\left(\hat{z}-\hat{h}_1\right)\right]\cosh\left[\eta\left(\hat{z}+\hat{h}_1+2\hat{h}_2\right)\right]\right\} \\
&\quad \times\left\{\cos\left[2\eta\left(\hat{h}_1+\hat{h}_2\right)\right]-\cosh\left[2\eta\left(\hat{h}_1+\hat{h}_2\right)\right]\right\}^{-1}, \qquad (20)
\end{aligned}
$$

$$
\begin{aligned}
W_4 &= \left\{-\cos\left[\eta\left(\hat{z}+\hat{h}_2\right)\right]\cosh\left[\eta\left(\hat{z}-2\hat{h}_1-\hat{h}_2\right)\right]\right. \\
&\quad \left.+\cos\left[\eta\left(\hat{z}-2\hat{h}_1-\hat{h}_2\right)\right]\cosh\left[\eta\left(\hat{z}+\hat{h}_2\right)\right]\right\} \\
&\quad \times\left\{\cos\left[2\eta\left(\hat{h}_1+\hat{h}_2\right)\right]-\cosh\left[2\eta\left(\hat{h}_1+\hat{h}_2\right)\right]\right\}^{-1}, \qquad (21)
\end{aligned}
$$

$$
\begin{aligned}
W_5 &= \left\{\sin\left[\eta\left(\hat{z}+\hat{h}_1+2\hat{h}_2\right)\right]\sinh\left[\eta\left(\hat{z}-\hat{h}_1\right)\right]\right. \\
&\quad \left.-\sin\left[\eta\left(\hat{z}-\hat{h}_1\right)\right]\sinh\left[\eta\left(\hat{z}+\hat{h}_1+2\hat{h}_2\right)\right]\right\} \\
&\quad \times\left\{\cos\left[2\eta\left(\hat{h}_1+\hat{h}_2\right)\right]-\cosh\left[2\eta\left(\hat{h}_1+\hat{h}_2\right)\right]\right\}^{-1}, \qquad (22)
\end{aligned}
$$

and

$$
\begin{aligned}
W_6 &= \left\{-\sin\left[\eta\left(\hat{z}+\hat{h}_2\right)\right]\sinh\left[\eta\left(\hat{z}-2\hat{h}_1-\hat{h}_2\right)\right]\right. \\
&\quad \left.+\sin\left[\eta\left(\hat{z}-2\hat{h}_1-\hat{h}_2\right)\right]\sinh\left[\eta\left(\hat{z}+\hat{h}_2\right)\right]\right\} \\
&\quad \times\left\{\cos\left[2\eta\left(\hat{h}_1+\hat{h}_2\right)\right]-\cosh\left[2\eta\left(\hat{h}_1+\hat{h}_2\right)\right]\right\}^{-1}, \qquad (23)
\end{aligned}
$$

in which the dimensionless electric potential $\hat{\psi}$ is given by Eq. (9). On integrating the axial velocity across the section, the primary (axial) flow rate is obtained as below:

$$
\begin{aligned}
\hat{q}_x &= \int_{-\hat{h}_2}^{\hat{h}_1}\hat{u}\,\mathrm{d}\hat{z} \\
&= -\frac{\hat{P}_x}{2\eta^3 E_1}-\left(\frac{\hat{\kappa}^3}{\hat{\kappa}^4+4\eta^4}\right)\tanh\left[\frac{\hat{\kappa}}{2}\left(\hat{h}_1+\hat{h}_2\right)\right]\left(\hat{\zeta}_1+\hat{\zeta}_2\right) \\
&\quad +\left[\frac{\hat{\kappa}^4}{2\eta\left(\hat{\kappa}^4+4\eta^4\right)}\right]\left(\frac{E_2}{E_1}\right)\left(\hat{\zeta}_1+\hat{\zeta}_2\right)-\left(\frac{\eta\hat{\kappa}^2}{\hat{\kappa}^4+4\eta^4}\right)\frac{\hat{\zeta}_1+\hat{\zeta}_2}{E_1}, \qquad (24)
\end{aligned}
$$

in which

$$
E_1=\frac{\cos\left[\eta\left(\hat{h}_1+\hat{h}_2\right)\right]+\cosh\left[\eta\left(\hat{h}_1+\hat{h}_2\right)\right]}{\sin\left[\eta\left(\hat{h}_1+\hat{h}_2\right)\right]-\sinh\left[\eta\left(\hat{h}_1+\hat{h}_2\right)\right]}, \qquad (25)
$$

and

$$
E_2=\frac{\sin\left[\eta\left(\hat{h}_1+\hat{h}_2\right)\right]+\sinh\left[\eta\left(\hat{h}_1+\hat{h}_2\right)\right]}{\sin\left[\eta\left(\hat{h}_1+\hat{h}_2\right)\right]-\sinh\left[\eta\left(\hat{h}_1+\hat{h}_2\right)\right]}. \qquad (26)
$$

On rearranging Eq. (24), we get

$$\begin{aligned}\frac{\hat{P}_x}{2\eta^2} &= -\eta\hat{q}_x E_1 - \left[\frac{\eta\hat{\kappa}^3 E_1}{\hat{\kappa}^4+4\eta^4}\right]\tanh\left[\frac{\hat{\kappa}}{2}\left(\hat{h}_1+\hat{h}_2\right)\right]\left(\hat{\zeta}_1+\hat{\zeta}_2\right) \\ &\quad + \left[\frac{\hat{\kappa}^4 E_2}{2\left(\hat{\kappa}^4+4\eta^4\right)}\right]\left(\hat{\zeta}_1+\hat{\zeta}_2\right) - \left(\frac{\eta^2\hat{\kappa}^2}{\hat{\kappa}^4+4\eta^4}\right)\left(\hat{\zeta}_1+\hat{\zeta}_2\right). \qquad (27)\end{aligned}$$

The wall shapes and potentials, $\hat{h}_{1,2}(\hat{x})$ and $\hat{\zeta}_{1,2}(\hat{x})$, are periodic functions of $\hat{x}$, and so are $E_{1,2}$. The flow rate $\hat{q}_x$ is, however, independent of $\hat{x}$, a consequence of continuity. The pressure gradient $\hat{P}_x$ consists of two components: a known constant (corresponding to the externally applied pressure gradient), and an unknown periodic function of $\hat{x}$ (corresponding to the internally induced pressure gradient). The spatial average of the latter component is zero by virtue of periodicity. Hence, on integrating the pressure gradient over one wavelength, we get

$$\langle\hat{P}_x\rangle = \int_0^1 \hat{P}_x \mathrm{d}\hat{x} = \Delta P, \qquad (28)$$

where ΔP is the net pressure drop in one period length of the channel. This pressure drop is simply equal to the applied pressure gradient multiplied by the wavelength of the wall pattern.

We then integrate Eq. (27) with respect to $\hat{x}$ from 0 to 1, and get after some algebra

$$\begin{aligned}\hat{q}_x &= \left\{-\frac{\Delta P}{2\eta^3} - \frac{\eta\hat{\kappa}^2}{\hat{\kappa}^4+4\eta^4}\int_0^1\left(\hat{\zeta}_1+\hat{\zeta}_2\right)\mathrm{d}\hat{x} + \frac{\hat{\kappa}^4}{2\eta\left(\hat{\kappa}^4+4\eta^4\right)}\int_0^1 E_2\left(\hat{\zeta}_1+\hat{\zeta}_2\right)\mathrm{d}\hat{x}\right. \\ &\quad \left. -\frac{\hat{\kappa}^3}{\hat{\kappa}^4+4\eta^4}\int_0^1 E_1\left(\hat{\zeta}_1+\hat{\zeta}_2\right)\tanh\left[\frac{\hat{\kappa}}{2}\left(\hat{h}_1+\hat{h}_2\right)\right]\mathrm{d}\hat{x}\right\}\Bigg/\int_0^1 E_1\mathrm{d}\hat{x}. \qquad (29)\end{aligned}$$

Substituting $\hat{q}_x$ back into Eq. (27), we then obtain the pressure gradient $\hat{P}_x$. With the known $\hat{P}_x$, we may finally obtain from Eqs. (16) and (17) the axial and transverse velocity components.

The secondary (transverse) flow rate, averaged over one wavelength, can then be found

as follows:

$$\begin{aligned}
\hat{q}_y &= \int_0^1 \int_{-\hat{h}_2}^{\hat{h}_1} \hat{v}(\hat{x},\hat{z})\,\mathrm{d}\hat{z}\,\mathrm{d}\hat{x} \\
&= \left\{\int_0^1 \left[E_1\eta\left(\hat{h}_1+\hat{h}_2\right)-E_2\right]\mathrm{d}\hat{x}\right\}\hat{q}_x - \frac{\hat{\kappa}^4}{\eta\left(\hat{\kappa}^4+4\eta^4\right)}\int_0^1 E_3\left(\hat{\zeta}_1+\hat{\zeta}_2\right)\mathrm{d}\hat{x} \\
&\quad - \frac{\hat{\kappa}}{\hat{\kappa}^4+4\eta^4}\int_0^1 \left(E_2\hat{\kappa}^2+2\eta^2\right)\left(\hat{\zeta}_1+\hat{\zeta}_2\right)\tanh\left[\frac{\hat{\kappa}}{2}\left(\hat{h}_1+\hat{h}_2\right)\right]\mathrm{d}\hat{x} \\
&\quad + \frac{\eta\hat{\kappa}^3}{\hat{\kappa}^4+4\eta^4}\int_0^1 E_1\left(\hat{h}_1+\hat{h}_2\right)\left(\hat{\zeta}_1+\hat{\zeta}_2\right)\tanh\left[\frac{\hat{\kappa}}{2}\left(\hat{h}_1+\hat{h}_2\right)\right]\mathrm{d}\hat{x} \\
&\quad + \frac{\hat{\kappa}^2}{2\left(\hat{\kappa}^4+4\eta^4\right)}\int_0^1 \left(2\eta^2-E_2\hat{\kappa}^2\right)\left(\hat{h}_1+\hat{h}_2\right)\left(\hat{\zeta}_1+\hat{\zeta}_2\right)\mathrm{d}\hat{x}, \qquad (30)
\end{aligned}$$

where

$$E_3 = \frac{\cos\left[\eta\left(\hat{h}_1+\hat{h}_2\right)\right]-\cosh\left[\eta\left(\hat{h}_1+\hat{h}_2\right)\right]}{\sin\left[\eta\left(\hat{h}_1+\hat{h}_2\right)\right]-\sinh\left[\eta\left(\hat{h}_1+\hat{h}_2\right)\right]}, \qquad (31)$$

and E_1 and E_2 are given in Eqs. (25) and (26), respectively.

Note that both $\hat{q}_x$ and $\hat{q}_y$ are separable into hydrodynamic and electrokinetic components, where the former is driven by the pressure drop ΔP, and the latter is controlled by the wall potentials $\hat{\zeta}_1+\hat{\zeta}_2$. The integrals in Eqs. (29) and (30) suggest possible interactions between the geometrical and potential variations on the walls.

3 Discussion

To facilitate our discussions, let us introduce the following sinusoidal functions for the wall shapes and potentials:

$$\hat{h}_1(\hat{x}) = 1 + h_1'\cos(2\pi\hat{x}), \qquad (32)$$

$$\hat{h}_2(\hat{x}) = 1 + h_2'\cos(2\pi\hat{x}+\phi), \qquad (33)$$

$$\hat{\zeta}_1(\hat{x}) = \bar{\zeta}_1 + \zeta_1'\cos(2\pi\hat{x}+\theta_1), \qquad (34)$$

$$\hat{\zeta}_2(\hat{x}) = \bar{\zeta}_2 + \zeta_2'\cos(2\pi\hat{x}+\theta_2), \qquad (35)$$

where $h_{1,2}'$ and $\zeta_{1,2}'$ are the amplitudes of the geometrical and potential variations on the upper/lower walls, $\bar{\zeta}_{1,2}$ are the mean potentials on the two walls, and ϕ and $\theta_{1,2}$ are the phase

shifts of the corresponding distributions. In the following, the geometrical and potential variations on the walls will be denoted by

$$\Delta\hat{h}(\hat{x}) \equiv \hat{h}(\hat{x}) - 1, \qquad \Delta\hat{\zeta}(\hat{x}) \equiv \hat{\zeta}(\hat{x}) - \bar{\zeta}. \tag{36}$$

In addition to these amplitudes and phase shifts pertaining to the wall undulation and surface potential distributions, the present problem is also controlled by the rotation parameter η, the Debye parameter $\hat{\kappa}$, and the pressure drop ΔP. While the Debye parameter is a ratio of the channel height to the EDL thickness, the rotation parameter can also be interpreted as a ratio of two lengths. From Eq. (15), η can be written as

$$\eta = h_0/\delta_E, \tag{37}$$

where

$$\delta_E = (\mu/\rho\Omega)^{1/2} \tag{38}$$

is the thickness of the Ekman layer, which is a boundary layer resulting from a balance between the Coriolis and viscous forces [38, 39]. Hence, the rotation parameter η is a ratio of the channel height to the Ekman layer thickness. Clearly, a faster rotation results in a thinner Ekman layer, thereby a larger η. It is of interest to provide some typical values for parameters considered in this study. In practice, the rotation speed of a centrifuge can be $O(10^3)$ rpm or faster and the dimension of a microchannel is typically $h_0 \sim 100$ μm. For a common liquid like water with the density $\rho \sim 10^3$ kg·m^{-3} and the dynamic viscosity $\mu \sim 10^{-3}$ Pa·s, the magnitude of the rotation parameter η can be as large as $O(10)$. Another dimensionless parameter of importance is the normalized Debye parameter $\hat{\kappa}$. The shielding thickness of the EDL (κ^{-1}) is typically in the range of 10 nm to 10 μm. Consequently, it is reasonable for us to choose $\hat{\kappa} = \kappa h_0 \sim O(10)$ in the following discussions.

3.1 Non-rotating channel

When the channel is not rotating ($\eta = 0$), the secondary flow is identically zero ($\hat{v} \equiv 0$). Let us distinguish quantities pertinent to a non-rotating channel by a superscript of "0". The axial velocity can be readily found from Eq. (13) as

$$\hat{u}^0 = \frac{\hat{P}_x^0}{2}\left(\hat{h}_1 - \hat{z}\right)\left(\hat{z} + \hat{h}_2\right) - \hat{\psi} + \left(\frac{\hat{z} + \hat{h}_2}{\hat{h}_1 + \hat{h}_2}\right)\hat{\zeta}_1 + \left(\frac{\hat{h}_1 - \hat{z}}{\hat{h}_1 + \hat{h}_2}\right)\hat{\zeta}_2, \tag{39}$$

where the electric potential $\hat{\psi}$ is given by Eq. (9). The corresponding pressure gradient and flow rate can be obtained as

$$\begin{aligned}\hat{P}_x^0 &= 12\hat{q}_x^0\left(\hat{h}_1+\hat{h}_2\right)^{-3}-6\left(\hat{\zeta}_1+\hat{\zeta}_2\right)\left(\hat{h}_1+\hat{h}_2\right)^{-2} \\ &\quad+\frac{12}{\hat{\kappa}}\left(\hat{\zeta}_1+\hat{\zeta}_2\right)\left(\hat{h}_1+\hat{h}_2\right)^{-3}\tanh\left[\frac{\hat{\kappa}}{2}\left(\hat{h}_1+\hat{h}_2\right)\right], \end{aligned} \tag{40}$$

$$\begin{aligned}\hat{q}_x^0 &= \left\{\frac{\Delta P}{12}-\frac{1}{\hat{\kappa}}\left\langle\left(\hat{\zeta}_1+\hat{\zeta}_2\right)\left(\hat{h}_1+\hat{h}_2\right)^{-3}\tanh\left[\frac{\hat{\kappa}}{2}\left(\hat{h}_1+\hat{h}_2\right)\right]\right\rangle\right. \\ &\quad\left.+\frac{1}{2}\left\langle\left(\hat{\zeta}_1+\hat{\zeta}_2\right)\left(\hat{h}_1+\hat{h}_2\right)^{-2}\right\rangle\right\}\Bigg/\left\langle\left(\hat{h}_1+\hat{h}_2\right)^{-3}\right\rangle, \end{aligned} \tag{41}$$

where the angle brackets denote averaging over one wavelength in the axial direction.

If $\hat{\kappa}\to\infty$, corresponding to the limiting case in which the EDL becomes infinitesimally thin, we may apply the Helmholtz–Smoluchowski slip condition directly on the boundary, which will avoid the need to include the electric body force in the momentum equation. In this limiting case, Eq. (41) reduces to

$$\lim_{\hat{\kappa}\to\infty}\hat{q}_x^0=\left[\Delta P+6\left\langle\left(\hat{\zeta}_1+\hat{\zeta}_2\right)\left(\hat{h}_1+\hat{h}_2\right)^{-2}\right\rangle\right]\Bigg/\left\langle 12\left(\hat{h}_1+\hat{h}_2\right)^{-3}\right\rangle, \tag{42}$$

which agrees with the one deduced previously by Qi and Ng [35], who considered EO flow of a power-law fluid in a non-rotating slit channel with gradually varied channel height and wall potential. Their analysis was also based on the lubrication approximation and the Helmholtz–Smoluchowski slip condition.

For sufficiently large $\hat{\kappa}$ such that $\tanh[\hat{\kappa}(\hat{h}_1+\hat{h}_2)/2]\approx 1$, we may substitute Eqs. (32)–(35) into Eq. (41), and get after some algebra the following analytical expression for the flow rate:

$$\hat{q}_x^0=\frac{A^{5/2}}{6C}\Delta P+\left[\frac{2A}{C}-\frac{1}{\hat{\kappa}}\right]\left(\bar{\zeta}_1+\bar{\zeta}_2\right)+\left[-A+\frac{6}{\hat{\kappa}}\right]\frac{B}{C}\qquad\text{for }\hat{\kappa}\gg 1, \tag{43}$$

where

$$A=4-h_1'^2-h_2'^2-2h_1'h_2'\cos(\phi), \tag{44}$$

$$\begin{aligned}B &= 2\left\langle\left(\Delta\hat{h}_1+\Delta\hat{h}_2\right)\left(\Delta\hat{\zeta}_1+\Delta\hat{\zeta}_2\right)\right\rangle \\ &= h_1'[\zeta_1'\cos(\theta_1)+\zeta_2'\cos(\theta_2)]+h_2'[\zeta_1'\cos(\phi-\theta_1)+\zeta_2'\cos(\phi-\theta_2)], \end{aligned} \tag{45}$$

and

$$C = 8 + h_1'^2 + h_2'^2 + 2h_1'h_2' \cos(\phi). \tag{46}$$

Equation (43) reveals that part of the flow rate can be due to various interactions between the geometrical variations (h_1', h_2') and the potential variations (ζ_1', ζ_2') on the walls.

3.2 Constant cross-sectional area

Here, we consider the special case in which the cross-sectional area of the channel is a constant, i.e., $\hat{h}_1 + \hat{h}_2 \equiv 2$. This means that either both walls are flat ($h_1' = h_2' = 0$), or the wall undulations have the same amplitude ($h_1' = h_2'$) and a phase shift of $\phi = \pi$ (i.e., synchronized undulations). Quantities pertinent to the present case are distinguished by a dagger.

When $\hat{h}_1 + \hat{h}_2 = 2$, Eqs. (29), (30) and (27) reduce, respectively, to

$$\hat{q}_x^\dagger = -\frac{\Delta P}{2E_1^\dagger \eta^3} + \left[-\hat{\kappa}\tanh(\hat{\kappa}) - \frac{\eta}{E_1^\dagger} + \frac{\hat{\kappa}^2 E_2^\dagger}{2\eta E_1^\dagger}\right] \frac{\hat{\kappa}^2\left(\bar{\zeta}_1 + \bar{\zeta}_2\right)}{\hat{\kappa}^4 + 4\eta^4}, \tag{47}$$

$$\begin{aligned} \hat{q}_y^\dagger &= \left(\frac{E_2^\dagger}{E_1^\dagger} - 2\eta\right)\left(\frac{\Delta P}{2\eta^3}\right) \\ &\quad + \left[-2\eta^2\tanh(\hat{\kappa}) + \frac{\hat{\kappa}^3}{2\eta E_1^\dagger} + \frac{\eta\hat{\kappa}E_2^\dagger}{E_1^\dagger}\right] \frac{\hat{\kappa}\left(\bar{\zeta}_1 + \bar{\zeta}_2\right)}{\hat{\kappa}^4 + 4\eta^4}, \end{aligned} \tag{48}$$

$$\hat{P}_x^\dagger = \Delta P - \left[\eta\hat{\kappa}E_1^\dagger \tanh(\hat{\kappa}) + \eta^2 - \frac{\hat{\kappa}^2 E_2^\dagger}{2}\right] \frac{2\eta^2\hat{\kappa}^2\left(\Delta\hat{\zeta}_1 + \Delta\hat{\zeta}_2\right)}{\hat{\kappa}^4 + 4\eta^4}, \tag{49}$$

where $\Delta\hat{\zeta}_{1,2} = \hat{\zeta}_{1,2} - \bar{\zeta}_{1,2}$, and

$$E_1^\dagger = \frac{\cos(2\eta) + \cosh(2\eta)}{\sin(2\eta) - \sinh(2\eta)} \quad \text{and} \quad E_2^\dagger = \frac{\sin(2\eta) + \sinh(2\eta)}{\sin(2\eta) - \sinh(2\eta)}. \tag{50}$$

Again, we see that the flow rates are each separable into a hydrodynamic component that is linearly proportional to the pressure drop ΔP, and an EO component that is in direct proportion to the wall potentials $\bar{\zeta}_1 + \bar{\zeta}_2$.

It is remarkable that the flow rates $\hat{q}_x^\dagger$ and $\hat{q}_y^\dagger$ are independent of the variations $\Delta\hat{h}_{1,2}$ and $\Delta\hat{\zeta}_{1,2}$, irrespective of these variations being zero or not. In other words, as long as the channel height is a constant, the primary and secondary flow rates will not be affected by any

non-uniformity in the wall shape and potential distribution. Under this particular condition, the interactions between the geometrical and potential variations, $\Delta\hat{h}$ and $\Delta\hat{\zeta}$, will have no contribution to the flow rates. This statement also applies to the case of flat walls (i.e., $h_1' = h_2' = 0$). Chang and Wang [12] have studied rotating EO flow between two parallel flat plates with an equal and uniform potential ζ on the walls. We here show that their flow rates will remain unchanged even when the two wall potentials are disparate and non-uniformly distributed, as long as the uniform potential is equal to the mean of the potential distributions: $\zeta = (\bar{\zeta}_1 + \bar{\zeta}_2)/2$. In this regard, the EO components of $\hat{q}_x^\dagger$ and $\hat{q}_y^\dagger$ can be checked to be in agreement with the real and imaginary parts of the complex flow rate deduced by Chang and Wang [12].

On the other hand, the internally induced pressure gradient is only incurred by the varying components of the wall potentials:

$$\begin{aligned} \Delta\hat{\zeta}_1 + \Delta\hat{\zeta}_2 &= \left(\hat{\zeta}_1 - \bar{\zeta}_1\right) + \left(\hat{\zeta}_2 - \bar{\zeta}_2\right) \\ &= \zeta_1' \cos(2\pi\hat{x} + \theta_1) + \zeta_2' \cos(2\pi\hat{x} + \theta_2), \end{aligned} \tag{51}$$

which will vanish when either $\zeta_1' = \zeta_2' = 0$ or $\zeta_1' = \zeta_2'$ and $|\theta_1 - \theta_2| = \pi$. Therefore, when the potential variations have the same amplitude and a phase shift of π, the induced pressure gradient, which varies periodically with axial position, will be identically zero, leaving behind only the externally applied pressure gradient.

3.3 Very thin Ekman and EDL layers

When the Ekman layer and EDL are both very thin, or $\eta \gg 1$ and $\hat{\kappa} \gg 1$, the interactions among the viscous force, electric force, Coriolis force and pressure gradient will be confined to a very thin near-wall layer, the so-called Ekman–EDL layer [9]. Outside this layer, the viscous and electric forces vanish, and the flow arises merely from a balance between the Coriolis force and the pressure gradient; this region is often called the geostrophic inviscid core. In what follows, quantities pertaining to the present case are distinguished by an asterisk.

In order to examine details in the Ekman–EDL layers, two stretched local coordinates are

introduced:

$$z_1^* = \eta\left(\hat{h}_1 - \hat{z}\right), \quad \text{and} \quad z_2^* = \eta\left(\hat{z} + \hat{h}_2\right), \tag{52}$$

which measure distance into the fluid from the upper and lower walls, respectively. While the Ekman–EDL layer lies in the region $z_{1,2}^* = O(1)$, the geostrophic interior is located where $z_{1,2}^* > O(1)$. We further introduce a modified dimensionless Debye parameter, which is the Debye parameter normalized by the Ekman layer thickness instead of the channel height, defined as follows:

$$\kappa^* = \hat{\kappa}/\eta = \kappa\delta_E, \tag{53}$$

where δ_E is the Ekman layer thickness given in Eq. (38). Here, $\kappa^* = O(1)$ is assumed.

In terms of z_1^* and z_2^*, the expressions for W_1–W_6, given in Eqs. (18)–(23), greatly simplify to the following, where the upper/lower functions are for the upper/lower Ekman–EDL layers:

$$W_1^* = \begin{cases} -\sin\left(z_1^*\right) e^{-z_1^*} \\ -\sin\left(z_2^*\right) e^{-z_2^*} \end{cases}, \tag{54}$$

$$W_2^* = \begin{cases} \cos\left(z_1^*\right) e^{-z_1^*} \\ \cos\left(z_2^*\right) e^{-z_2^*} \end{cases}, \tag{55}$$

$$W_3^* = \begin{cases} \cos\left(z_1^*\right) e^{-z_1^*} \\ 0 \end{cases}, \tag{56}$$

$$W_4^* = \begin{cases} 0 \\ \cos\left(z_2^*\right) e^{-z_2^*} \end{cases}, \tag{57}$$

$$W_5^* = \begin{cases} -\sin\left(z_1^*\right) e^{-z_1^*} \\ 0 \end{cases}, \tag{58}$$

$$W_6^* = \begin{cases} 0 \\ -\sin\left(z_2^*\right) e^{-z_2^*} \end{cases}. \tag{59}$$

Also, the electric potential ψ^* and the pressure gradient P_x^* can be written as

$$\psi^* = \begin{cases} \hat{\zeta}_1 e^{-\kappa^* z_1^*} & \text{near the upper wall} \\ \hat{\zeta}_2 e^{-\kappa^* z_2^*} & \text{near the lower wall} \end{cases}, \tag{60}$$

$$\frac{P_x^*}{2\eta^2} = \frac{\Delta P}{2\eta^2} - \frac{\kappa^{*2}\left(\kappa^{*2} - 2\kappa^* + 2\right)}{2\left(\kappa^{*4} + 4\right)}\left(\Delta\hat{\zeta}_1 + \Delta\hat{\zeta}_2\right), \tag{61}$$

where $\Delta\hat{\zeta}_1 + \Delta\hat{\zeta}_2$ is the sum of the wall potential variations, as in Eq. (51). While W_1^*–W_6^* and ψ^* are all zero in the geostrophic core, P_x^* is independent of vertical position.

Then, the axial and transverse velocities, given in Eqs. (16) and (17), simplify to

$$u_1^* = -\frac{\kappa^{*4}\hat{\zeta}_1 e^{-\kappa^* z_1^*}}{\kappa^{*4}+4} + \frac{\kappa^{*2}\hat{\zeta}_1 e^{-z_1^*}}{\kappa^{*4}+4}\left[\kappa^{*2}\cos(z_1^*) + 2\sin(z_1^*)\right] + \sin(z_1^*)\, e^{-z_1^*}\left(\frac{P_x^*}{2\eta^2}\right), \tag{62}$$

$$v_1^* = -\frac{2\kappa^{*2}\hat{\zeta}_1 e^{-\kappa^* z_1^*}}{\kappa^{*4}+4} + \frac{\kappa^{*2}\hat{\zeta}_1 e^{-z_1^*}}{\kappa^{*4}+4}\left[-\kappa^{*2}\sin(z_1^*) + 2\cos(z_1^*)\right] + \left[\cos(z_1^*)\, e^{-z_1^*} - 1\right]\left(\frac{P_x^*}{2\eta^2}\right), \tag{63}$$

for the upper Ekman–EDL layer, and

$$u_2^* = -\frac{\kappa^{*4}\hat{\zeta}_2 e^{-\kappa^* z_2^*}}{\kappa^{*4}+4} + \frac{\kappa^{*2}\hat{\zeta}_2 e^{-z_2^*}}{\kappa^{*4}+4}\left[\kappa^{*2}\cos(z_2^*) + 2\sin(z_2^*)\right] + \sin(z_2^*)\, e^{-z_2^*}\left(\frac{P_x^*}{2\eta^2}\right), \tag{64}$$

$$v_2^* = -\frac{2\kappa^{*2}\hat{\zeta}_2 e^{-\kappa^* z_2^*}}{\kappa^{*4}+4} + \frac{\kappa^{*2}\hat{\zeta}_2 e^{-z_2^*}}{\kappa^{*4}+4}\left[-\kappa^{*2}\sin(z_2^*) + 2\cos(z_2^*)\right] + \left[\cos(z_2^*)\, e^{-z_2^*} - 1\right]\left(\frac{P_x^*}{2\eta^2}\right), \tag{65}$$

for the lower Ekman–EDL layer, where $(P_x^*/2\eta^2)$ is given by Eq. (61). Here, we see that part of the flow in each Ekman-EDL layer is due to the pressure gradient that is incurred by the variations of the wall potentials. This internally induced pressure gradient, which varies periodically with axial position, is locally uniform across the entire channel section, including the Ekman–EDL layers and the geostrophic core. Because of this pressure gradient, the velocity of flow in the upper Ekman–EDL layer is controlled not only by the potential $\hat{\zeta}_1$ on the upper wall, but also by the potential variation $\Delta\hat{\zeta}_2$ on the lower wall. It is remarkable that, even though the two Ekman–EDL layers are far apart from each other, the variation of potential on one wall will have effect on the flow near the other wall. Such dependence of flow in one Ekman–EDL layer on the boundary condition in the other Ekman–EDL layer will happen as long as the wall potentials are non-uniformly distributed.

From Eqs. (62)–(65), the asymptotic limits for velocities outside the Ekman–EDL layer are readily found as

$$u^* = \lim_{z_1^*\to\infty} u_1^* = \lim_{z_2^*\to\infty} u_2^* = 0, \tag{66}$$

$$\begin{aligned} v^* = \lim_{z_1^*\to\infty} v_1^* = \lim_{z_2^*\to\infty} v_2^* &= -\frac{P_x^*}{2\eta^2} \\ &= -\frac{\Delta P}{2\eta^2} + \frac{\kappa^{*2}\left(\kappa^{*2} - 2\kappa^* + 2\right)}{2\left(\kappa^{*4}+4\right)}\left(\Delta\hat{\zeta}_1 + \Delta\hat{\zeta}_2\right), \end{aligned} \tag{67}$$

which are the axial and transverse flow velocities in the geostrophic core. As noted above, the geostrophic core is a region where the viscous and electric forces are zero. Hence, with these forcings vanishing, the axial and transverse momentum equations, as in Eqs. (1) and (2), reduce to

$$-2\rho\Omega v = P_x, \qquad 2\rho\Omega u = 0. \tag{68}$$

Obviously, the solution to the above equations is simply $u = 0$ and $v = -P_x/(2\rho\Omega)$, or in terms of dimensionless variables, $u^* = 0$ and $v^* = -P_x^*/2\eta^2$. This accords with the limiting velocities obtained above. A more formal proof (e.g., Pedlosky [39]) shows that the velocity in the geostrophic core is in general given by

$$\vec{u}_\perp = \frac{\vec{k} \times \nabla p}{2\rho\Omega}, \tag{69}$$

where $\vec{k}$ is the unit vector along the axis of rotation, and $\vec{u}_\perp$ is the geostrophic velocity, which is always perpendicular to $\vec{k}$ and the pressure gradient ∇p. In the present problem, the pressure gradient is non-zero in the x-direction, but is zero in the y-direction. Consequently, the geostrophic velocity is non-zero in the y-direction, but is zero in the x-direction. The y-component geostrophic velocity v^*, given in Eq. (67), depends on the following: ΔP, η, κ^*, and $\Delta\hat{\zeta}_1 + \Delta\hat{\zeta}_2$. If the latter is not zero, it varies also periodically with $\hat{x}$.

For illustration, we show in Fig. 2 some velocity profiles, $u_1^*(z_1^*)$ and $v_1^*(z_1^*)$, in the upper Ekman–EDL layer at $\hat{x} = 0$, where $\Delta P = 0$, $\bar{\zeta}_1 = 1$, $\kappa^* = 1$, $\zeta_1' = 0$, and $\zeta_2' = 0.5$. For these parameter values, $\Delta\hat{\zeta}_1 = 0$ (i.e., uniform potential distribution on the upper wall), and $\Delta\hat{\zeta}_2 = 0.5\cos(\theta_2)$. We can clearly see from this figure how the phase θ_2 of the lower wall potential variation can change the velocity profiles in the upper Ekman–EDL layer. Outside the Ekman–EDL layer, as $z_1^* \gg 1$, the velocity profiles will tend to the geostrophic limits given in Eqs. (66)–(67): $u_1^* \to 0$, $v_1^* \to \kappa^{*2}(\kappa^{*2} - 2\kappa^* + 2)\zeta_2' \cos(\theta_2)/2(\kappa^{*4} + 4) = 0.05\cos(\theta_2)$. The axial velocity profiles of u_1^* shown in Fig. 2(a) exhibit an oscillatory behavior about the zero value when z_1^* increases from zero ($z_1^* = 0$ refers to the upper wall). The axial velocity increases sharply and reaches the positive maximum near the wall due to the pumping EO effect, then reduces to be negative maximum in the region where the adverse Coriolis effect dominates over the aiding EO effect, and eventually diminishes outside the Ekman–EDL layer. If the system rotation is fast enough, such oscillatory profiles are often seen, as have been reported by Qi and Ng [16].

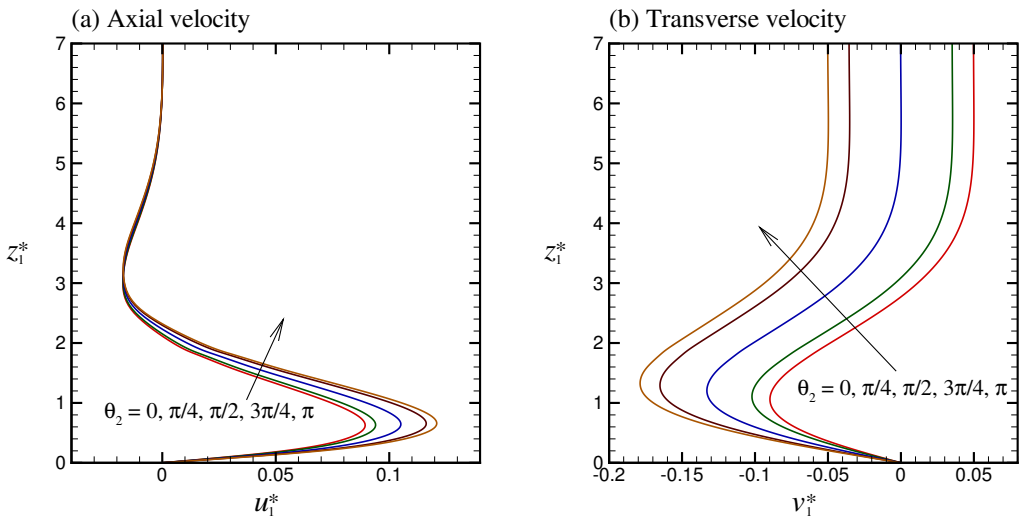

Figure 2: Axial and transverse velocity profiles, $u_1^*(z_1^*)$ and $v_1^*(z_1^*)$, in the upper Ekman–EDL layer at $\hat{x} = 0$ for various θ_2, where $\Delta P = 0$, $\bar{\zeta}_1 = \kappa^* = 1$, $\zeta_1' = 0$, and $\zeta_2' = 0.5$. The velocity profiles asymptotically tend to the geostrophic limits given in Eqs. (66)–(67) as $z_1^* \gg 1$.

It is of interest to examine the axial and transverse flow rates when $\hat{\kappa}$ and η are both large and comparable to each other. From the velocity profiles given in Eqs. (62)–(65), we can get

$$\begin{aligned} q_x^* &= \int_0^{\hat{h}_1} u_1^* \mathrm{d}\hat{z} + \int_{-\hat{h}_2}^0 u_2^* \mathrm{d}\hat{z} \\ &= \frac{1}{\eta}\int_0^{\eta\hat{h}_1} u_1^* \mathrm{d}z_1^* + \frac{1}{\eta}\int_0^{\eta\hat{h}_2} u_2^* \mathrm{d}z_2^* \\ &= \frac{\Delta P}{2\eta^3} + \frac{\kappa^{*2}\left(\kappa^{*2} - 2\kappa^* + 2\right)}{2\eta\left(\kappa^{*4} + 4\right)}\left(\bar{\zeta}_1 + \bar{\zeta}_2\right), \end{aligned} \tag{70}$$

$$\begin{aligned} q_y^* &= \left\langle \int_0^{\hat{h}_1} v_1^* \mathrm{d}\hat{z} + \int_{-\hat{h}_2}^0 v_2^* \mathrm{d}\hat{z} \right\rangle \\ &= \left\langle \frac{1}{\eta}\int_0^{\eta\hat{h}_1} v_1^* \mathrm{d}z_1^* + \frac{1}{\eta}\int_0^{\eta\hat{h}_2} v_2^* \mathrm{d}z_2^* \right\rangle \\ &= \left[\frac{1}{\eta} - \left(\bar{h}_1 + \bar{h}_2\right)\right]\frac{\Delta P}{2\eta^2} - \frac{\kappa^*\left(\kappa^{*3} - 2\kappa^* + 4\right)}{2\eta\left(\kappa^{*4} + 4\right)}\left(\bar{\zeta}_1 + \bar{\zeta}_2\right) \\ &\quad + \frac{\kappa^{*2}\left(\kappa^{*2} - 2\kappa^* + 2\right)}{2\left(\kappa^{*4} + 4\right)}\left\langle\left(\Delta\hat{h}_1 + \Delta\hat{h}_2\right)\left(\Delta\hat{\zeta}_1 + \Delta\hat{\zeta}_2\right)\right\rangle, \end{aligned} \tag{71}$$

where the angle brackets denote averaging over one wavelength in the x-direction, $\bar{h}_1 = \bar{h}_2 = 1$, and $\Delta\hat{h}$ and $\Delta\hat{\zeta}$ are the geometrical and potential variations as defined in Eq. (36). As

has already been given by Eq. (45), the angle-bracketed term in the last line of the above equation can be written as follows:

$$\left\langle \left(\Delta\hat{h}_1 + \Delta\hat{h}_2\right)\left(\Delta\hat{\zeta}_1 + \Delta\hat{\zeta}_2\right)\right\rangle = B/2$$
$$= \left\{h_1'[\zeta_1'\cos(\theta_1) + \zeta_2'\cos(\theta_2)] + h_2'\left[\zeta_1'\cos(\phi-\theta_1) + \zeta_2'\cos(\phi-\theta_2)\right]\right\}/2. \quad (72)$$

Several points about the two flow rates are noteworthy. First, the primary flow rate q_x^* depends only on the mean wall potentials $\bar{\zeta}_1 + \bar{\zeta}_2$, and is unaffected by the variation in the wall shape or potential. The secondary flow rate q_y^* depends not only on the mean wall potentials, but also on the interaction between $\Delta\hat{h}_{1,2}$ and $\Delta\hat{\zeta}_{1,2}$. Second, the term that is proportional to the sum of the mean potentials $(\bar{\zeta}_1 + \bar{\zeta}_2)$ will diminish with increasing rotation speed according to η^{-1}. In sharp contrast, the term that is proportional to $\langle(\Delta\hat{h}_1 + \Delta\hat{h}_2)(\Delta\hat{\zeta}_1 + \Delta\hat{\zeta}_2)\rangle$ can remain finite even when $\eta \gg 1$, as long as $\kappa^* = O(1)$. Third, the hydrodynamic component that is proportional to ΔP will diminish with increasing rotation speed according to η^{-3} for the primary flow, but only according to η^{-2} for the secondary flow. The second and third points are related to the geostrophic limits discussed above. Equations (70) and (71) suggest that the primary flow rate will diminish more rapidly than the secondary flow rate as the rotation speed increases. Also, at very high rotation speed, the primary flow rate will become virtually zero, while the secondary flow rate can remain finite, where the finite limit depends on the interaction between $\Delta\hat{h}$ and $\Delta\hat{\zeta}$. A possibly non-zero finite limit of secondary flow at high rotation speed is a feature that distinguishes rotating EO flow in a non-uniform channel from that in a uniform channel.

3.4 Uncharged flat lower wall

We here consider the case with the following wall shape and potential distributions: $\hat{h}_1(\hat{x}) = 1 + 0.5\cos(2\pi\hat{x})$, $\hat{\zeta}_1(\hat{x}) = \cos(2\pi\hat{x} + \theta_1)$, $\hat{h}_2 = 1$, and $\hat{\zeta}_2 = 0$, corresponding to a flat and uncharged lower wall. The average potential $\bar{\zeta}_1$ on the upper wall is also zero. Therefore, over one half period the potential is positive, and over the other half period the potential is negative. Such symmetry in positive and negative potential distributions will result in a net zero flux in an otherwise uniform channel. A non-zero flux is possible only when the symmetry is broken. Here, the symmetry can be broken because of the variation in the wall

height. Let us consider the following two limiting cases. First, for a very thin EDL and zero rotation, the axial EO flow rate can be obtained from Eq. (43) as follows:

$$\hat{q}_x^0 = \frac{[-(4-h_1'^2)+6/\hat{\kappa}]h_1'\zeta_1'\cos(\theta_1)}{8+h_1'^2} \qquad \text{for } \Delta P = 0,\ \hat{\kappa} \gg 1,\ \eta = 0. \tag{73}$$

Second, for a very thin EDL and high speed rotation, the transverse EO flow rate can be obtained from Eq. (71) as follows:

$$q_y^* = \frac{\kappa^{*2}(\kappa^{*2}-2\kappa^*+2)h_1'\zeta_1'\cos(\theta_1)}{4(\kappa^{*4}+4)} \qquad \text{for } \Delta P = 0,\ \hat{\kappa} \gg 1,\ \eta \gg 1. \tag{74}$$

In the above equations, h_1' and ζ_1' are the amplitudes of the geometrical and potential variations on the upper wall. The two flow rates are non-zero as long as $\zeta_1' h_1' \cos(\theta_1) \neq 0$. In other words, as long as $\cos(\theta_2) \neq 0$, the interaction between $\Delta\hat{h}$ and $\Delta\hat{\zeta}$ can lead to a non-zero flow, although the average potential is zero. Note that $\hat{q}_x^0$ is negative when $\theta_1 = 0$, and is positive when $\theta_1 = \pi$. This is due to fact that flow through a channel with transverse wall patterns is always rate controlled by the cross-section with the largest resistance; see e.g., Ng and Zhou [33]. When $\theta_1 = 0$, the potential is the maximum negative at $\hat{x} = 1/2$, where the cross-section is the narrowest or the height is the smallest $\hat{h}_1 = 1 - h_1'$. The resultant axial flow rate is therefore negative. The opposite is true for $\theta_1 = \pi$, for which the potential is the maximum positive at the narrowest section at $\hat{x} = 1/2$, thereby resulting in a positive axial flow rate. In case $\theta_1 = \pi/2$, the symmetry remains unbroken, and hence the flow rate is zero.

These effects of θ_1 on the flow rate remain qualitatively unchanged in the presence of system rotation. As shown in Fig. 3, for any rotation parameter η, the axial flow rate is negative in the range $0 \leq \theta_1 < \pi/2$, and is positive in the range $\pi/2 < \theta_1 \leq \pi$. The opposite is true for the transverse flow rate, which is always opposite in sign to the axial flow rate. Since the mean potential is zero, it is therefore the wall potential around the narrowest cross-section that determines the primary flow rate. The primary flow rate will decrease monotonically as the rotation parameter η increases, and is nearly zero when $\eta = 5$. The secondary flow rate will first increase, attaining its maximum at $\eta \approx 1$, before it decreases as η increases. Such a trend has been reported previously by Chang and Wang [12]. Note that the values of $\hat{\kappa} = \eta = 10$ are already large enough for $\hat{q}_y$ to get very close to the limit given by Eq. (74). The results shown in Fig. 3 confirm our earlier remark: as $\eta \gg 1$, $\hat{q}_x$ tends to zero, while $\hat{q}_y$ tends to a finite limit owing to the interaction between $\Delta\hat{h}$ and $\Delta\hat{\zeta}$.

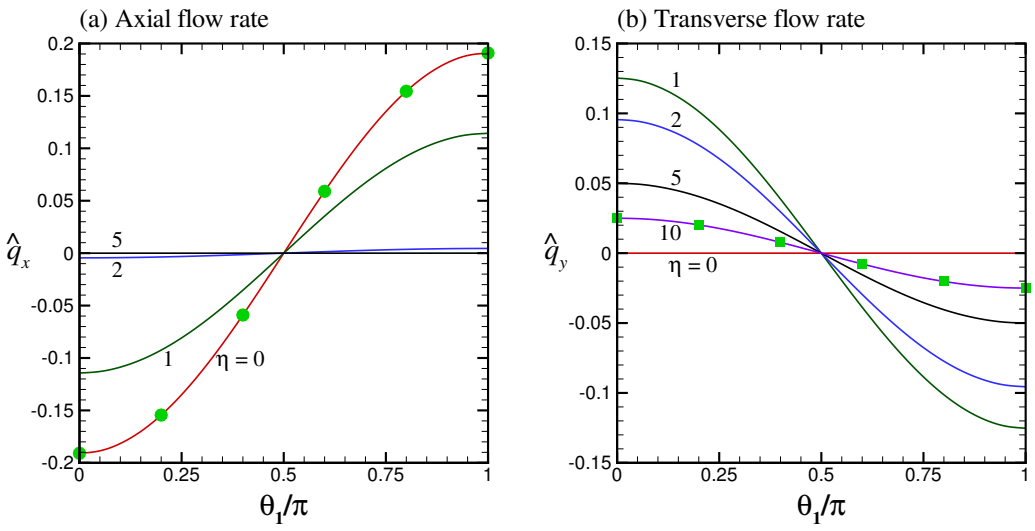

Figure 3: Axial and transverse flow rates as functions of the phase θ_1 for various η, where $\Delta P = 0$, $\hat{\kappa} = 10$, $h_1' = 0.5$, $\bar{\zeta}_1 = 0$, $\zeta_1' = 1$, and $h_2' = \bar{\zeta}_2 = \zeta_2' = 0$ (uncharged flat lower wall). In (a), the symbols are from Eq. (73). In (b), the symbols are from Eq. (74), which is valid for $\eta \gg 1$.

3.5 Symmetrical wall patterns

We first consider the following wall shape and potential distributions:

$$\hat{h}_1(\hat{x}) = \hat{h}_2(\hat{x}) = 1 + h' \cos(2\pi\hat{x}), \qquad \hat{\zeta}_1(\hat{x}) = \hat{\zeta}_2(\hat{x}) = \cos(2\pi\hat{x} + \pi). \tag{75}$$

Let us find out how the geometrical amplitude h' will affect the flow. Again, the average potential on either wall is zero. Therefore, to generate non-zero flow, variation in channel height is needed in order to break the symmetry. Here, the phase $\theta_1 = \theta_2 = \pi$. As has been pointed out above, for this phase shift, the net primary flow is positive while the secondary flow is negative. At one extreme, the flow rate is zero when $h' = 0$, as the mechanism to break the symmetry disappears. At the other extreme, the flow rate is also zero when $h' = 1$, as the channel is completely closed at the narrowest cross-section. This implies that the flow rate should vary with h' in a non-monotonic manner. This also implies the existence of an optimum amplitude $0 < h_{\rm m}' < 1$ at which the flow rate is maximum.

In Figs. 4(a,b), we show the axial and transverse flow rates as functions of h' for $\eta =$ 0, 1, 2, 5, where $\Delta P = 0$ and $\kappa = 10$. Increasing h' has two opposite effects on the flow: one

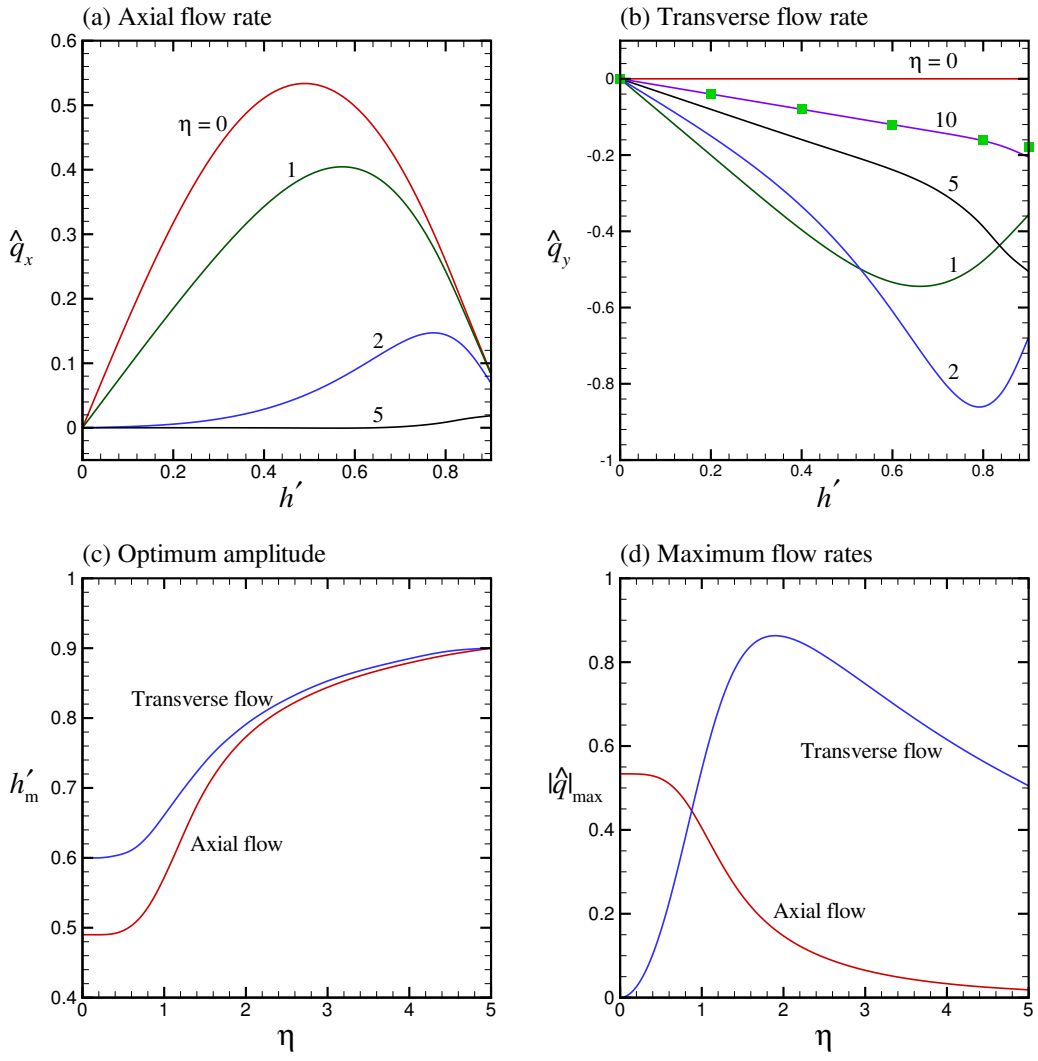

Figure 4: In (a, b), axial and transverse flow rates as functions of the geometrical amplitude h' for various η, where $\Delta P = 0$, $\hat{\kappa} = 10$, and the wall shape and potential distributions are given by Eq. (75). In (c, d), optimum amplitude $h'_{\rm m}$ and corresponding maximum flow rates as functions of the rotation parameter η. In (b), the symbols are from Eq. (71), which is valid for $\eta \gg 1$.

is to strength the mechanism to break the symmetry, and one is to decrease the cross-sectional area of the narrowest section. When h' is small, the former effect dominates, and hence the effect is favorable. When h' is large (close to unity), the latter effect dominates, and hence the effect is adverse. This explains the non-monotonic behaviors exhibited by the curves shown in Figs. 4(a,b). The optimum amplitude $h'_{\rm m}$ and the corresponding maximum flow rate $|\hat{q}|_{\rm max}$ are functions of the rotation parameter η, as shown in Figs. 4(c,d). The optimum amplitude for the transverse flow is somewhat larger than that for the axial flow. Also, the maximum axial flow rate decreases monotonically with increasing η, while the maximum transverse flow rate will attain a peak value at $\eta \approx 2$. In Fig. 4(b), we see again that the transverse flow rate $\hat{q}_y$ at $\eta = 10$ is very close to the limiting value given by Eq. (71), except when h' is close to unity.

We next consider the following wall shape and potential distributions:

$$\hat{h}_1(\hat{x}) = \hat{h}_2(\hat{x}) = 1 + 0.5\cos(2\pi\hat{x}), \qquad \hat{\zeta}_1(\hat{x}) = \hat{\zeta}_2(\hat{x}) = 1 + \zeta'\cos(2\pi\hat{x}). \tag{76}$$

Let us examine here the effect of the potential amplitude ζ' on the flow. We show in Fig. 5 the axial and transverse flow rates as functions of the rotation parameter η for $\zeta' = 0, 0.5, 1, 1.5, 2$, where $\Delta P = 0$ and $\hat{\kappa} = 10$. Chang and Wang [12] have shown that, under the action of a positive uniform wall potential, the axial and transverse flow rates are, respectively, positive and negative. Also, the axial flow rate will decrease monotonically with the rotation rate, while the transverse flow rate will attain a maximum when the rotation rate is order unity. Figure 5 reveals that these trends still hold for non-uniform wall potential as long as the amplitude ζ' is not too large. When the amplitude becomes so large that it is comparable to the mean, $\zeta' \sim \bar{\zeta}$, such that the potential is nearly zero or even negative over part of the distribution, qualitatively different trends are exhibited. First, the axial flow rate no longer decreases monotonically with increasing rotation rate. Instead, $\hat{q}_x$ will first increase to attain a maximum before it decreases as η increases. This can be reasoned as follows. Owing to the smallest (or even negative) potential being located at the narrowest section, the interaction between $\Delta\hat{h}$ and $\Delta\hat{\zeta}$ is to reduce the primary flow rate when the rotation parameter is zero or small. Figure 5(a) clearly shows that $\hat{q}_x$ decreases sharply as ζ' increases at $\eta = 0$. At higher η, the system rotation tends to weaken the reducing effect due to the interaction between $\Delta\hat{h}$ and $\Delta\hat{\zeta}$ on $\hat{q}_x$. Therefore, for any $\zeta' > 0$, the curve will asymptotically approach that

for $\zeta' = 0$ as $\eta \to \infty$. This leads to the rise before the decline of the curves for the case $\zeta' > \bar{\zeta}$. The effect of ζ' on $\hat{q}_x$ is already very small when $\eta = 5$. This is consistent with our earlier finding that, as $\eta \gg 1$, the geometrical or potential variations, h' or ζ', will lose influence on the axial flow rate $\hat{q}_x$. Second, the transverse flow rate is no longer negative when ζ' is sufficiently large. It happens that $\hat{q}_x$ and $\hat{q}_y$ can be both positive for a sufficiently large amplitude ζ'. This stands in sharp contrast to the case of a uniform potential, for which the two flow rates are always opposite in sign (in the sense of the right-hand rule). We may see from Fig. 5(b) that the transverse flow rate is most sensitively affected by the amplitude ζ' when the rotation parameter $\eta \approx 1$. This means that, at $\eta = O(1)$, varying ζ' can dramatically change $\hat{q}_y$, not only the magnitude but also the direction of flow. Again, at $\eta = 10$, $\hat{q}_y$ gets very close to the limiting value given by Eq. (71).

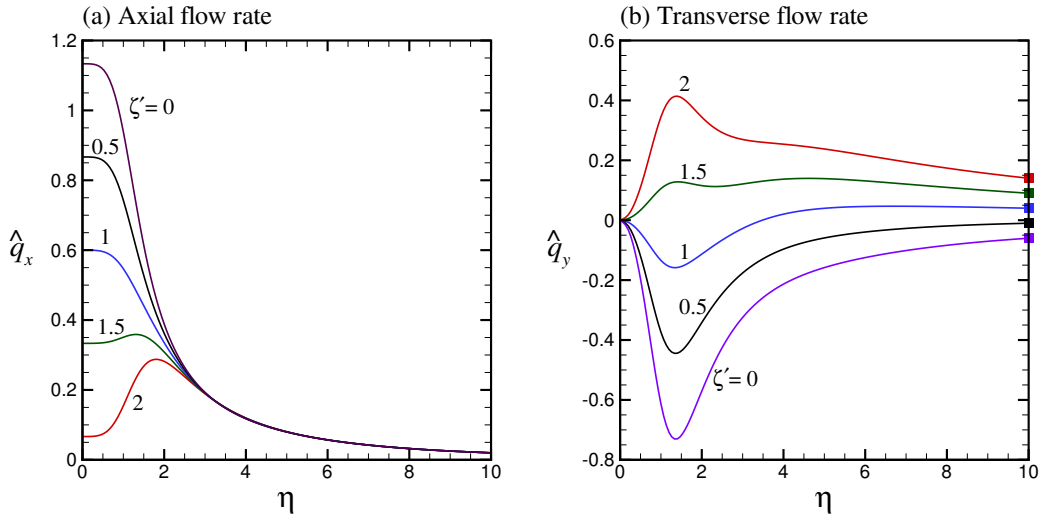

Figure 5: Axial and transverse flow rates as function of the rotation parameter η for various ζ', where $\Delta P = 0$, $\hat{\kappa} = 10$, and the wall shape and potential distributions are given by Eq. (76). In (b), the symbols are from Eq. (71), which is valid for $\eta \gg 1$.

4 Concluding remarks

Fluid flow in microchannels on a rotating disk is controlled mainly by the spinning speed of the disk. By introducing electrokinetics into a rotating flow through a non-uniform channel,

the system may admit more controlling factors such as electrostatic force and induced pressure gradient, in addition to the centrifugal and Coriolis pseudo-forces. The utilization of various geometrical, kinematic and electric effects will allow for a more flexible design for fluidic transport in a narrow confinement. This study is the first analytical study that aims to look into the combined effects due to these effects on rotating electroosmotic flow.

Applying the lubrication approximation, we have obtained analytical solutions for the primary and secondary flow fields of rotating electroosmotic flow in a narrow slit microchannel, where the wall shape and wall potential may vary slowly in the direction of the applied fields. We have looked into various cases of particular interest to find out how the primary and secondary flows are affected by the controlling parameters, including the rotation and Debye parameters, and the amplitudes and phase shifts of the wall shape and potential distributions. Some key findings are summarized as follows. Depending on the phase shifts, there can be various interactions between the geometrical and potential variations on the upper and lower walls, and these interactions may materially modify the velocity and pressure fields within a certain range of the rotation speed. An exception happens when the wall undulations are synchronized, for which the flow rates will not be affected by the geometrical and potential variations. For the limiting case of large rotation and Debye parameters, or the case of very thin Ekman and EDL layers, asymptotic analysis has been carried out to determine the velocity profiles in the Ekman–EDL layer in terms of the modified Debye parameter. It is found that, although the two Ekman–EDL layers that develop near the walls are far away from each other, the potential variation on one wall can have effect on the flow near the other wall. The interaction between the geometrical and potential variations can produce a net flow even when the mean potential is zero, but such effect on the primary flow will be weakened by the system rotation. Secondary flow rate typically attains its maximum and is also most sensitively affected by the interaction between the geometrical and potential variations when the rotation parameter is order unity. Furthermore, the secondary flow rate tends to decrease more slowly with increasing rotation parameter than the primary flow rate. It is possible that non-uniformity in the wall shape and potential distribution may lead to a non-zero limiting secondary flow rate at large rotation speed. This is in sharp contrast to the case of uniform flow, for which the secondary flow can only diminish to zero at large rotation

speed. Our work has revealed that varying the amplitudes and phase shifts of the geometrical and potential variations on the walls may dramatically change the effect of system rotation on the primary and secondary flow rates.

The scope of this study was limited to relatively simple geometries and mild variations such that the flow is quasi-parallel to the walls, and the Reynolds number is so low that the lubrication approximation can be applied. Notwithstanding these limitations, this work offers valuable insight into how wall patterning may be manipulated in order to enrich the flow behaviors for electrokinetic transport in centrifugal microfluidics. It is desirable if experiments can be conducted in the future to test and verify these theoretical findings. It is envisaged that theoretical modeling and laboratory work can go hand-in-hand to enhance our understanding of electroosmotic flow in a rotating microchannel with axial non-uniformity. Many details in terms of the fundamental physics and practical implications deserve to be further investigated.

Compliance with Ethical Standards

Funding: This study was funded by the Research Grants Council of the Hong Kong Special Administrative Region, China, through General Research Fund Project No. 17206615.

Conflict of Interest: The authors declare that they have no conflict of interest.

References

[1] Wang X, Cheng C, Wang S, Liu S (2009) Electroosmotic pumps and their applications in microfluidic systems. Microfluid Nanofluid 6:145–162

[2] Jakeway SC, de Mello AJ, Russell EL (2000) Miniaturized total analysis systems for biological analysis. Fresen J Anal Chem 366:525–539

[3] Whitesides GM, Stroock DA (2001) Flexible methods for microfluidics. Phys Today 54:42–48

[4] Ren L, Qu W, Li D (2001) Interfacial electrokinetic effects on liquid flow in microchannels. Int J Heat Mass Transf 44:3125–3134

[5] Probstein RF (1994) Physicochemical hydrodynamics: an introduction, 2nd edn. John Wiley & Sons, New York. ISBN 0-471-01011-1

[6] Hunter RJ (1981) Zeta potential in colloid science: principles and applications. Academic Press, London. ISBN 0123619602

[7] Everett DH (1988) Basic principles of colloid science. Royal Society of Chemistry, London. ISBN 978-1-84755-020-0

[8] Madou M, Zoval J, Jia G, Kido H, Kim J, Kim N (2006) Lab on a CD. Annu Rev Biomed Eng 8:601–628

[9] Ng CO, Qi C (2015) Electro-osmotic flow in a rotating rectangular microchannel. Proc R Soc A 471:20150200

[10] Wang GJ, Hsu WH, Chang YZ, Yang H (2004) Centrifugal and electric field forces dual-pumping CD-like microfluidic platform for biomedical separation. Biomed Microdevices 6:47–53

[11] Chakraborty S (2013) Microfluidics and microscale transport processes. CRC Press, Boca Raton. ISBN 978-1-4398-9924-3

[12] Chang CC, Wang CY (2011) Rotating electro-osmotic flow over a plate or between two plates. Phys Rev E 84:056320

[13] Xie ZY, Jian YJ (2014) Rotating electroosmotic flow of power-law fluids at high zeta potentials. Colloids Surf A: Physicochem Eng Asp 461:231–239

[14] Li SX, Jian YJ, Xie ZY, Liu QS, Li FQ (2015) Rotating electro-osmotic flow of third grade fluids between two microparallel plates. Colloids Surf A: Physicochem Eng Asp 470:240–247

[15] Abhimanyu P, Kaushik P, Mondal PK, Chakraborty S (2016) Transiences in rotational electro-hydrodynamics microflows of a viscoelastic fluid under electrical double layer phenomena. J Non-Newtonian Fluid Mech 231:56–67

[16] Qi C, Ng CO (2017) Rotating electroosmotic flow of viscoplastic material between two parallel plates. Colloids Surf A: Physicochem Eng Asp 513:355–366

[17] Qi C, Ng CO (2017) Rotating electroosmotic flow of an Eyring fluid. Acta Mech Sin 33:295–315

[18] Kaushik P, Mondal PK, Chakraborty S (2017) Rotational electrohydrodynamics of a non-Newtonian fluid under electrical double-layer phenomenon: the role of lateral confinement. Microfluid Nanofluid 21:122

[19] Kaushik P, Abhimanyu P, Mondal PK, Chakraborty S (2017) Confinement effects on the rotational microflows of a viscoelastic fluid under electrical double layer phenomenon. J Non-Newtonian Fluid Mech 244:123–137

[20] Kaushik P, Mondal S, Chakraborty S (2017) Transient electroosmosis of a Maxwell fluid in a rotating microchannel. Electrophoresis doi:10.1002/elps.201700090

[21] Towns JK, Regnier FE (1991) Capillary electrophoretic separations of proteins using nonionic surfactant coatings. Anal Chem 91:1126–1132

[22] Towns JK, Regnier FE (1992) Impact of polycation adsorption on efficiency and electroosmotically driven transport in capillary electrophoresis. Anal Chem 64:2473–2478

[23] Hu Y, Werner C, Li D (2003) Electrokinetic transport through rough microchannels. Anal Chem 75:5747–5758

[24] Chang CC, Yang RJ (2004) Computational analysis of electrokinetically driven flow mixing in microchannels with patterned blocks. J Micromech Microeng 14:550–558

[25] Stroock AD, Weck M, Chiu DT, Huck WTS, Kenis PJA, Ismagilov RF, Whitesides GM (2000) Patterning electro-osmotic flow with patterned surface charge. Phys Rev Lett 85:3314–3317

[26] Ajdari A (1995) Electro-osmosis on inhomogeneously charged surfaces. Phys Rev Lett 75:755–758

[27] Ajdari A (1996) Generation of transverse fluid currents and forces by an electric field: electro-osmosis on charge-modulated and undulated surfaces. Phys Rev E 53:4996–5005

[28] Yang D, Liu Y (2008) Numerical simulation of electroosmotic flow in microchannels with sinusoidal roughness. Colloids Surf A: Physicochem Eng Asp 328:28–33

[29] Shit GC, Mondal A, Sinha A, Kundu PK (2016) Effects of slip velocity on rotating electro-osmotic flow in a slowly varying micro-channel. Colloids Surf A: Physicochem Eng Asp 489:249–255

[30] Long D, Stone HA, Ajdari A (1999) Electroosmotic flows created by surface defects in capillary electrophoresis. J Colloid Interface Sci 212:338–349

[31] Ajdari A (2001) Transverse electrokinetic and microfluidic effects in micropatterned channels: Lubrication analysis for slab geometries. Phys Rev E 65:016301

[32] Ghosal S (2002) Lubrication theory for electro-osmotic flow in microfluidic channel of slowly varying cross-section and wall charge. J Fluid Mech 459:103–128

[33] Ng CO, Zhou Q (2012) Electro-osmotic flow through a thin channel with gradually varying wall potential and hydrodynamic slippage. Fluid Dyn Res 44:055507

[34] Ng CO, Zhou Q (2014) Electroosmotic flow of a power-law fluid in a non-uniform microchannel. J Non-Newtonian Fluid Mech 208–209:118–125

[35] Qi C, Ng CO (2015) Electroosmotic flow of a power-law fluid through an asymmetrical slit microchannel with gradually varying wall shape and wall potential. Colloid Surf A: Physicochem Eng Asp 472:26–37

[36] Qi C, Ng CO (2015) Electroosmotic flow of a power-law fluid in a slit microchannel with gradually varying channel height and wall potential. European J Mech B/Fluids 52:160–168

[37] Deen WM (2012) Analysis of transport phenomena, 2nd edn. Oxford University Press, New York. ISBN 978-0-19-974028-4

[38] Tritton DJ (1988) Physical fluid dynamics, 2nd edn. Clarendon Press, Oxford. ISBN 0-19-854489-8

[39] Pedlosky J (1987) Geophysical fluid dynamics, 2nd edn. Springer-Verlag, New York. ISBN 0-387-96387-1